

A Unified Fractional Spectral Framework for Spatiotemporal Graph Signals: Bi-Fractional Transform and Geodesic Coupling

Mingzhi Wang, Manjun Cui, Feiyue Zhao, Yangfan He, and Zhichao Zhang, *Member, IEEE*

Abstract—Graph signal processing extends spectral analysis to data supported on irregular domains. Existing fractional transforms for two-dimensional graph signals, including the two-dimensional graph fractional Fourier transform (GFRFT), typically impose a shared fractional order across dimensions, which limits adaptivity to heterogeneous spatiotemporal spectra. To address this limitation, we propose the two-dimensional graph bi-fractional Fourier transform, which assigns independent fractional orders to the factor graphs of a Cartesian product, enabling decoupled spectral control while preserving separability, unitarity, and invertibility. To further resolve the basis ambiguity in temporal fractional analysis, we develop a geodesic-coupled GFRFT by constructing a coupling path along the principal geodesic on the unitary manifold, thereby unifying graph-induced and discrete temporal bases with guaranteed unitarity and a closed-form inverse. Building on these transforms, we derive a differentiable Wiener-type filtering framework with a hybrid optimization strategy: the fractional orders are learned end-to-end from data, while the coupling parameter is fixed as a structural regularizer. Experiments on real-world time-varying graph datasets and dynamic image restoration tasks demonstrate consistent gains over state-of-the-art fractional transforms and competitive learning-based baselines.

Index Terms—Denoising, geodesic-coupled GFRFT, joint time-vertex fractional Fourier transform, two-dimensional GFRFT, two-dimensional graph bi-fractional Fourier transform.

I. INTRODUCTION

Signals originating from real-world systems are often supported on complex networks or graphs, thereby exhibiting non-Euclidean topologies. Representative examples include

This work was supported in part by the Open Foundation of Hubei Key Laboratory of Applied Mathematics (Hubei University) under Grant HBAM202404; in part by the Foundation of Key Laboratory of System Control and Information Processing, Ministry of Education under Grant Scip20240121; and in part by the Startup Foundation for Introducing Talent of Nanjing Institute of Technology under Grant YKJ202214. (*Corresponding author: Zhichao Zhang.*)

Mingzhi Wang, Manjun Cui, and Feiyue Zhao are with the School of Mathematics and Statistics, Nanjing University of Information Science and Technology, Nanjing 210044, China (e-mail: wzm200208@163.com; cmj1109@163.com; 202511150010@nuist.edu.cn).

Yangfan He is with the School of Communication and Artificial Intelligence, School of Integrated Circuits, Nanjing Institute of Technology, Nanjing 211167, China, and also with the Jiangsu Province Engineering Research Center of IntelliSense Technology and System, Nanjing 211167, China (e-mail: Yangfan.He@njit.edu.cn).

Zhichao Zhang is with the School of Mathematics and Statistics, Nanjing University of Information Science and Technology, Nanjing 210044, China, with the Hubei Key Laboratory of Applied Mathematics, Hubei University, Wuhan 430062, China, and also with the Key Laboratory of System Control and Information Processing, Ministry of Education, Shanghai Jiao Tong University, Shanghai 200240, China (e-mail: zzc910731@163.com).

spatiotemporal measurements from environmental sensing networks [1]–[3], interactions in social networks [4], [5], brain connectivity graphs in neuroscience [6], [7], and pixel- or region-level relations in image analysis [8]–[11]. The irregularity of these domains makes it difficult to directly apply classical techniques developed for Euclidean signals. Graph signal processing (GSP) provides a principled extension of traditional methodologies, including Fourier analysis [12]–[16], wavelet transforms [17]–[20], sampling theory [21]–[23], and filtering [12], [14], [16], [24]–[26], to signals defined on graphs, enabling efficient modeling and analysis on irregular topologies.

In GSP, the graph Fourier transform (GFT) represents signals in a spectral domain induced by the eigendecomposition of a graph operator. Common choices of spectral operators include the graph Laplacian and the adjacency matrix. The Laplacian emphasizes smoothness and is well suited to diffusion-type processes, whereas the adjacency matrix emphasizes connectivity and can better capture nonstationary behavior and localized high-frequency patterns [12], [13], [16], [27]. In this work, we adopt the adjacency matrix as the spectral operator to model signals with strong local variations. We focus on weighted undirected graphs so that the adjacency matrix admits an orthonormal eigendecomposition, yielding a unitary spectral basis. Despite its effectiveness, the GFT relies on fixed integer-order spectral modes, which limits its ability to adapt spectral representations to multiscale and heterogeneous structures.

To provide a continuous degree of freedom, the graph fractional Fourier transform (GFRFT) extends the GFT by introducing a fractional order that parameterizes a family of graph spectral transforms. Such representations have been applied to denoising, spectrum sparsification, and graph filtering [28]–[34]. In the classical fractional Fourier transform (FRFT), the fractional order is often interpreted via time-frequency rotation. This geometric interpretation does not directly carry over to graph settings because graph frequencies are induced by a chosen graph operator rather than Euclidean geometry. Accordingly, we treat the fractional order as a continuous spectral parameterization in the graph setting. Most existing GFRFT methods, however, focus on single-graph signals and provide limited support for multidimensional or multi-structure graph data.

Many applications naturally involve multidimensional graph signals, such as time-vertex or space-attribute data. Cartesian product graphs provide a convenient model for such joint

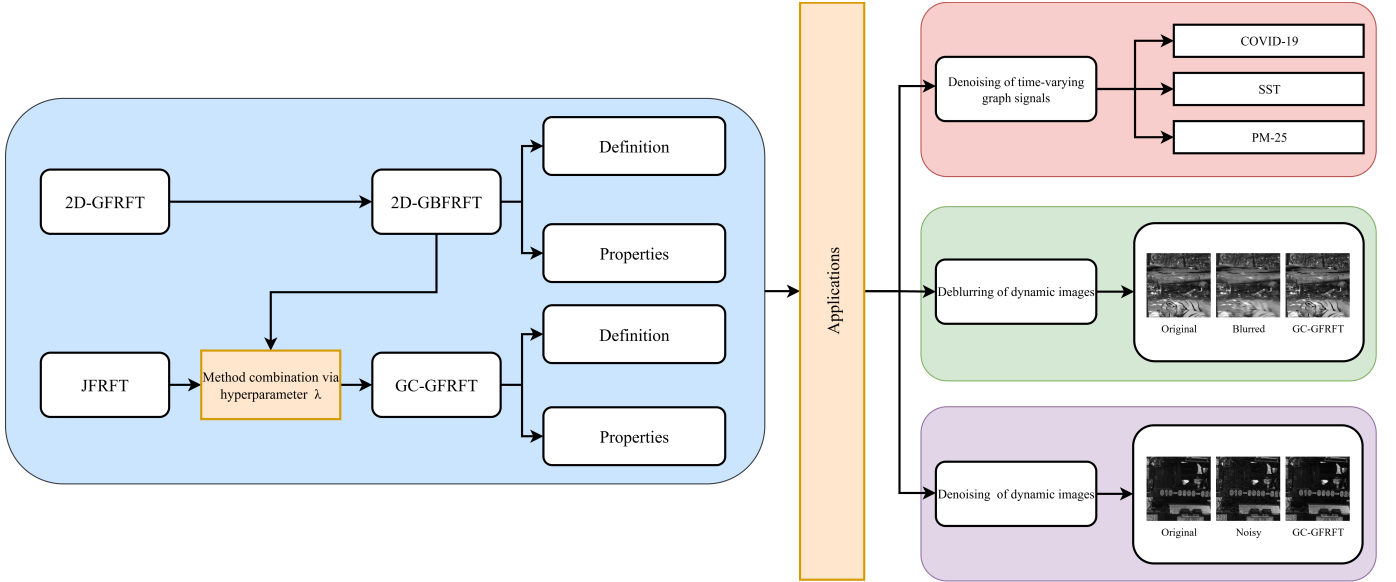


Fig. 1. Overview of the proposed GC-GFRFT framework and its applications.

structures by combining two factor graphs to represent multiway dependencies. Within this setting, the two-dimensional GFT (2D-GFT) performs spectral decompositions on the factor graphs and combines them through the Kronecker product, yielding a separable joint spectral representation with favorable computational properties [35]–[37]. Nonetheless, 2D-GFT remains restricted to integer-order descriptions. The two-dimensional GFRFT (2D-GFRFT) alleviates this limitation by applying a shared fractional order to both factor graphs [38]. This shared-order construction implicitly assumes that a single order can adequately control the two factor spectra. In strongly heterogeneous settings, such as when one dimension is relatively smooth while the other exhibits pronounced local variations, this constraint can significantly reduce expressiveness.

To address this limitation, we propose the two-dimensional graph bi-fractional Fourier transform (2D-GBFRFT). By assigning two independent fractional orders to the two factor graphs of a Cartesian product, the proposed bi-fractional design enables factor-wise tuning of the joint spectral coordinates. This improves modeling fidelity for heterogeneous two-dimensional graph signals while retaining the separable product-graph structure that supports efficient spectral-domain processing.

Beyond spatial heterogeneity, analyzing time-varying graph signals also requires selecting an appropriate temporal fractional basis. Joint spectral analysis is central to such signals, as exemplified by the joint time-vertex Fourier transform (JFT) [39], [40] and the joint time-vertex FRFT (JFRFT) [41]–[43]. In practical spatiotemporal settings, the temporal dimension can be modeled either by a graph-induced fractional transform associated with a temporal graph, such as a path graph, or by a classical discrete FRFT (DFRFT) basis. Although both choices are typically unitary and thus energy preserving, they can induce different temporal spectral coordinate systems, which in turn affect subsequent filtering and representation.

This observation motivates our second contribution: a structure-preserving coupling mechanism for heterogeneous temporal fractional bases. A naive Euclidean interpolation between two unitary operators, such as linear mixing, generally breaks unitarity and can lead to ill-conditioned transforms, which compromise energy preservation and stable reconstruction [44], [45]. Instead of interpolating in the ambient Euclidean space, we regard unitary operators as points on a Riemannian manifold and connect the two temporal endpoints through the principal geodesic [46]. The resulting one-parameter family, indexed by $\lambda \in [0, 1]$, remains unitary for all λ , and its inverse is given by the Hermitian transpose. This intrinsic construction motivates the term geodesic-coupled, abbreviated as GC, and we refer to the resulting framework as the GC-GFRFT.

Wiener filtering is a fundamental mean-squared error (MSE) denoising technique [16], [19], [47]–[49]. Its graph counterpart applies spectral attenuation in the GFT domain and acts as a linear minimum-MSE estimator under stochastic priors [50], [51]. To better align signal and noise spectra, GFRFT provides a tunable spectral domain. Early GFRFT-based filters derived their coefficients from prior statistical knowledge while using fixed fractional orders [47]. For time-varying signals, JFRFT-based filters employed grid search to optimize two hybrid fractional parameters, with a graph-induced basis used in the spatial domain and a discrete FRFT basis used in the temporal domain [41], [42]. However, such discrete parameter sweeps become computationally expensive as the dimensionality increases.

Recent differentiable GFRFT formulations overcome this by enabling gradient-based learning of fractional orders and filter parameters [31]. More broadly, learning-based filtering frameworks are actively advancing graph signal processing [52], leading to the exploration of learnable JFRFT designs for joint time-vertex spectral control [43]. These advances demonstrate that fractional-domain designs substantially enhance the

expressiveness of spectral denoising and shaping on graphs. Motivated by these advances and the fact that the temporal dimension admits two valid yet generally incompatible unitary fractional bases, we develop a differentiable Wiener-type filtering framework under a unified fractional spectral model. In our approach, the coupling parameter serves as a fixed structural regularizer selected via coarse search, while the fractional orders and diagonal spectral filters are learned end-to-end via gradient descent (GD).

In summary, we develop a unified fractional spectral framework for Cartesian product graphs and spatiotemporal graph signals. The main contributions are as follows:

- We propose 2D-GBFRFT, a separable transform on Cartesian product graphs with independent fractional orders on the two factor graphs, enabling dimension-wise adaptivity and clarifying its distinction from JFRFT by using graph-induced bases in both dimensions.
- We introduce GC-GFRFT, a unitary geodesic coupling that bridges the graph-induced temporal basis and the DFRFT basis with a closed-form inverse, unifying 2D-GBFRFT ($\lambda = 0$) and JFRFT ($\lambda = 1$) as endpoint cases.
- We develop a regularized learnable Wiener-type filtering scheme that learns the fractional orders and diagonal spectral filters by GD while treating λ as a fixed structural hyperparameter, and validate it on real data.

The remainder of this paper is organized as follows. Section II reviews the preliminaries, including the fundamentals of GSP, Cartesian product graphs, and existing fractional transforms. Section III proposes the 2D-GBFRFT, detailing its definition and theoretical properties. Section IV introduces the GC-GFRFT, which resolves the temporal basis ambiguity via geodesic coupling on the unitary manifold. Section V develops the differentiable Wiener filtering framework based on a hybrid optimization strategy. Section VI presents applications on real-world data, covering the denoising of time-varying graph signals and dynamic image restoration tasks. Finally, Section VII concludes the paper and outlines future research directions, and technical proofs are provided in the Appendix. Fig. 1 presents an overview of the proposed GC-GFRFT framework and its applications.

Notation: Bold lowercase letters denote vectors and bold uppercase letters denote matrices. The sets of real and complex numbers are denoted by \mathbb{R} and \mathbb{C} , respectively. For a set \mathcal{V} , $|\mathcal{V}|$ denotes its cardinality. The operators $(\cdot)^*$, $(\cdot)^T$, and $(\cdot)^H$ represent the complex conjugate, transpose, and Hermitian transpose, respectively. The identity matrix of size N is denoted by \mathbf{I}_N . The operator $\text{diag}(\mathbf{h})$ denotes the diagonal matrix whose diagonal entries are given by \mathbf{h} . The operator $\text{vec}(\cdot)$ denotes vectorization. The expectation operator is denoted by $\mathbb{E}\{\cdot\}$. The Euclidean (ℓ_2) norm and Frobenius norm are denoted by $\|\cdot\|_2$ and $\|\cdot\|_F$, respectively. The Kronecker product, Kronecker sum, and Hadamard product are denoted by \otimes , \oplus , and \circ , respectively.

II. PRELIMINARIES

A. Graph Signals

Let $G = (\mathcal{V}, \mathbf{A})$ be a weighted undirected graph, where $\mathcal{V} = \{v_1, v_2, \dots, v_N\}$ denotes the node set with cardinality $|\mathcal{V}| =$

N , and $\mathbf{A} \in \mathbb{R}^{N \times N}$ is the weighted adjacency matrix. An entry $\mathbf{A}_{ij} > 0$ indicates that an edge exists between nodes v_i and v_j with weight \mathbf{A}_{ij} , while $\mathbf{A}_{ij} = 0$ indicates the absence of an edge. A graph signal is a function $x : \mathcal{V} \rightarrow \mathbb{R}$ that assigns a scalar value x_i to each node $v_i \in \mathcal{V}$. The values of the signal are collected into the vector $\mathbf{x} = [x_1, x_2, \dots, x_N]^T \in \mathbb{R}^N$ [53], which represents the signal in the vertex domain, with structure governed by the connectivity encoded in \mathbf{A} .

To incorporate temporal dynamics, we assume that the graph signal is observed at T successive time instants with a unit sampling interval. Let $\mathbf{x}_t \in \mathbb{R}^N$ denote the signal at time t . The time-varying graph signal is represented by the matrix $\mathbf{X} = [\mathbf{x}_1, \mathbf{x}_2, \dots, \mathbf{x}_T] \in \mathbb{R}^{N \times T}$. Both \mathbf{X} and its vectorized form $\mathbf{x} = \text{vec}(\mathbf{X}) \in \mathbb{R}^{NT}$ are referred to as the time-vertex signal [54], [55].

A Cartesian product $G_1 \square G_2$ of two weighted graphs $G_1 = (\mathcal{V}_1, \mathcal{E}_1, \mathbf{A}_1)$ and $G_2 = (\mathcal{V}_2, \mathcal{E}_2, \mathbf{A}_2)$ is a graph with vertex set $\mathcal{V}_1 \times \mathcal{V}_2$. Its edge set \mathcal{E} is defined by

$$\{(i_1, i_2), (j_1, j_2)\} \in \mathcal{E} \iff [\{i_1, j_1\} \in \mathcal{E}_1, i_2 = j_2] \\ \text{or } [i_1 = j_1, \{i_2, j_2\} \in \mathcal{E}_2],$$

and the edge weight, corresponding to the entries of the adjacency matrix \mathbf{A} of $G_1 \square G_2$, is given by

$$[\mathbf{A}]_{(i_1, i_2), (j_1, j_2)} = [\mathbf{A}_1]_{i_1, j_1} \delta(i_2, j_2) + \delta(i_1, j_1) [\mathbf{A}_2]_{i_2, j_2}.$$

Graphs G_1 and G_2 are referred to as the factor graphs of $G_1 \square G_2$.

Let G_n with vertex set $\mathcal{V}_n = \{1, 2, \dots, N_n\}$ have adjacency, degree, and Laplacian matrices \mathbf{A}_n , \mathbf{D}_n , and \mathbf{L}_n , respectively, for $n = 1, 2$. When the vertices of the Cartesian product graph $\mathcal{V}_1 \times \mathcal{V}_2$ are ordered lexicographically, i.e., $(1, 1), (1, 2), \dots, (N_1, N_2)$, the adjacency, degree, and Laplacian matrices of $G_1 \square G_2$ can be written as $\mathbf{A}_1 \oplus \mathbf{A}_2$, $\mathbf{D}_1 \oplus \mathbf{D}_2$, and $\mathbf{L}_1 \oplus \mathbf{L}_2$, respectively [35].

B. 2D-GFRFT

We consider the adjacency matrix \mathbf{A}_n of a weighted graph G_n . For real symmetric weighted graphs, \mathbf{A}_n is diagonalizable with eigenvalue decomposition $\mathbf{\Lambda}_{A_n} = \mathbf{V}_{A_n}^H \mathbf{A}_n \mathbf{V}_{A_n}$, where \mathbf{V}_{A_n} contains the eigenvectors of \mathbf{A}_n and $\mathbf{\Lambda}_{A_n}$ is a diagonal matrix of eigenvalues. The GFT matrix is defined as $\mathbf{F}_{G_n} = \mathbf{V}_{A_n}^H$, and the inverse is given by $\mathbf{F}_{G_n}^{-1} = \mathbf{V}_{A_n}$ [13].

We define the GFRFT as

$$\mathbf{F}_{G_n}^{\alpha_n} = \mathbf{V}_{F_n} \mathbf{J}_{F_n}^{\alpha_n} \mathbf{V}_{F_n}^{-1}, \quad (1)$$

where $\mathbf{J}_{F_n}^{\alpha_n}$ represents the fractional matrix in the graph Fourier domain, and \mathbf{V}_{F_n} is the eigenvector matrix of \mathbf{F}_{G_n} . If \mathbf{F}_{G_n} is unitary, then $(\mathbf{F}_{G_n}^{\alpha_n})^H = \mathbf{F}_{G_n}^{-\alpha_n}$.

Given a graph signal $X : \mathcal{V}_1 \times \mathcal{V}_2 \rightarrow \mathbb{R}$ on the Cartesian product graph $G_1 \square G_2$, let $N_i \triangleq |\mathcal{V}_i|$ ($i = 1, 2$) and let $\mathbf{X} \in \mathbb{R}^{N_1 \times N_2}$ denote the vertex-domain matrix representation of X .

Definition 1: The 2D-GFRFT of \mathbf{X} is defined as

$$\mathbf{X}_f^\alpha = \mathbf{F}_{G_1}^\alpha \mathbf{X} (\mathbf{F}_{G_2}^\alpha)^T, \quad (2)$$

where $\mathbf{F}_{G_i}^\alpha$ ($i = 1, 2$) are the α -order GFRFT matrices of G_i . The inverse transform is

$$\mathbf{X} = \mathbf{F}_{G_1}^{-\alpha} \mathbf{X}_f^\alpha (\mathbf{F}_{G_2}^{-\alpha})^T. \quad (3)$$

Equivalently, in vectorized form, letting $\mathbf{x} \triangleq \text{vec}(\mathbf{X})$ and $\mathbf{x}_f^\alpha \triangleq \text{vec}(\mathbf{X}_f^\alpha)$, we have

$$\mathbf{x}_f^\alpha = (\mathbf{F}_{G_2}^\alpha \otimes \mathbf{F}_{G_1}^\alpha) \mathbf{x} \triangleq \mathbf{F}_{2D}^\alpha \mathbf{x}, \quad (4)$$

with the corresponding inverse

$$\mathbf{x} = (\mathbf{F}_{G_2}^{-\alpha} \otimes \mathbf{F}_{G_1}^{-\alpha}) \mathbf{x}_f^\alpha \triangleq \mathbf{F}_{2D}^{-\alpha} \mathbf{x}_f^\alpha. \quad (5)$$

The 2D-GFRFT thus provides a joint spectral representation spanned by the fractional eigenmodes of the two factor graphs and reduces to the classical 2D-GFT when $\alpha = 1$ [38].

C. JFRFT

The FRFT extends the classical Fourier transform by introducing a continuous order parameter α [56]–[58]. Its discrete version, known as the DFRFT, is represented by a matrix $\mathbf{F}^\alpha \in \mathbb{C}^{T \times T}$, which reduces to the discrete Fourier transform (DFT) when $\alpha = 1$ [59].

JFRFT generalizes this concept to time-varying graph signals, incorporating both the graph structure and temporal dynamics. Let $\mathbf{X} \in \mathbb{C}^{N \times T}$ denote a signal matrix defined over a graph with N vertices and T time instants, and let $\mathbf{x} = \text{vec}(\mathbf{X}) \in \mathbb{C}^{NT}$ be its vectorized form.

Definition 2: The JFRFT of \mathbf{X} is defined as

$$\mathbf{X}_J^{(\alpha, \beta)} = \mathbf{F}_G^\beta \mathbf{X} (\mathbf{F}^\alpha)^T, \quad (6)$$

where \mathbf{F}^α is the α -order DFRFT matrix, \mathbf{F}_G^β is the β -order GFRFT matrix, and $\mathbf{X}_J^{(\alpha, \beta)}$ denotes the JFRFT-domain representation of \mathbf{X} . The inverse transform is

$$\mathbf{X} = \mathbf{F}_G^{-\beta} \mathbf{X}_J^{(\alpha, \beta)} (\mathbf{F}^{-\alpha})^T. \quad (7)$$

Equivalently, in vectorized form, we have

$$\mathbf{x}_J^{(\alpha, \beta)} = (\mathbf{F}^\alpha \otimes \mathbf{F}_G^\beta) \mathbf{x} \triangleq \mathbf{F}_J^{(\alpha, \beta)} \mathbf{x}, \quad (8)$$

with the corresponding inverse

$$\mathbf{x} = (\mathbf{F}^{-\alpha} \otimes \mathbf{F}_G^{-\beta}) \mathbf{x}_J^{(\alpha, \beta)} \triangleq \mathbf{F}_J^{(-\alpha, -\beta)} \mathbf{x}_J^{(\alpha, \beta)}. \quad (9)$$

The JFRFT thus provides a joint fractional spectral representation of time-varying graph signals and reduces to the classical JFT when $\alpha = 1$ and $\beta = 1$.

III. TWO-DIMENSIONAL GRAPH BI-FRACTIONAL FOURIER TRANSFORM

A. Definition

The conventional 2D-GFRFT applies an identical fractional order to both factor graphs of a Cartesian product graph [38]. Although this uniform specification simplifies the transform, it may fail to capture structural heterogeneity between the two factors. In particular, when the factors exhibit significantly different characteristics, such as in space-time graph scenarios, a single shared order can introduce spectral aliasing or obscure directional information.

To overcome these limitations, we propose the 2D-GBFRFT. Unlike the conventional formulation, 2D-GBFRFT assigns two independent fractional orders, α_1 and α_2 , to the factor graphs, enabling adaptivity along each dimension. This bi-fractional design improves both the flexibility and fidelity

of spectral representations, particularly when the factor graphs have distinct structural properties.

Let two graphs be given as $G_1 = (\mathcal{V}_1, \mathcal{E}_1, \mathbf{A}_1)$ and $G_2 = (\mathcal{V}_2, \mathcal{E}_2, \mathbf{A}_2)$, with $N_1 = |\mathcal{V}_1|$ and $N_2 = |\mathcal{V}_2|$. Their adjacency matrices \mathbf{A}_1 and \mathbf{A}_2 admit the eigendecompositions

$$\mathbf{A}_1 = \mathbf{V}_{A_1} \mathbf{\Lambda}_1 \mathbf{V}_{A_1}^T, \quad \mathbf{A}_2 = \mathbf{V}_{A_2} \mathbf{\Lambda}_2 \mathbf{V}_{A_2}^T. \quad (10)$$

Given two independent fractional orders $\alpha_1, \alpha_2 \in \mathbb{R}$, the bi-fractional transform matrices are defined as

$$\mathbf{F}_{G_1}^{\alpha_1} = \mathbf{V}_{A_1} \mathbf{\Lambda}_1^{\alpha_1} \mathbf{V}_{A_1}^T, \quad \mathbf{F}_{G_2}^{\alpha_2} = \mathbf{V}_{A_2} \mathbf{\Lambda}_2^{\alpha_2} \mathbf{V}_{A_2}^T. \quad (11)$$

Given a graph signal $X : \mathcal{V}_1 \times \mathcal{V}_2 \rightarrow \mathbb{R}$ on the Cartesian product graph $G_1 \square G_2$, let $N_i \triangleq |\mathcal{V}_i|$ ($i = 1, 2$) and let $\mathbf{X} \in \mathbb{R}^{N_1 \times N_2}$ denote the vertex-domain matrix representation of X .

Definition 3: The 2D-GBFRFT of \mathbf{X} is defined as

$$\mathbf{X}_f^{\alpha_1, \alpha_2} = \mathbf{F}_{G_1}^{\alpha_1} \mathbf{X} (\mathbf{F}_{G_2}^{\alpha_2})^T, \quad (12)$$

where $\mathbf{F}_{G_i}^{\alpha_i}$ ($i = 1, 2$) denote the α_i -order GFRFT matrices of G_i , and $\mathbf{X}_f^{\alpha_1, \alpha_2}$ is the 2D-GBFRFT representation of \mathbf{X} . The inverse transform is

$$\mathbf{X} = \mathbf{F}_{G_1}^{-\alpha_1} \mathbf{X}_f^{\alpha_1, \alpha_2} (\mathbf{F}_{G_2}^{-\alpha_2})^T. \quad (13)$$

In vectorized form, letting $\mathbf{x} \triangleq \text{vec}(\mathbf{X})$ and $\mathbf{x}_f^{\alpha_1, \alpha_2} \triangleq \text{vec}(\mathbf{X}_f^{\alpha_1, \alpha_2})$, we have

$$\mathbf{x}_f^{\alpha_1, \alpha_2} = (\mathbf{F}_{G_2}^{\alpha_2} \otimes \mathbf{F}_{G_1}^{\alpha_1}) \mathbf{x} \triangleq \mathbf{F}_{2D}^{(\alpha_1, \alpha_2)} \mathbf{x}, \quad (14)$$

with the corresponding inverse

$$\mathbf{x} = (\mathbf{F}_{G_2}^{-\alpha_2} \otimes \mathbf{F}_{G_1}^{-\alpha_1}) \mathbf{x}_f^{\alpha_1, \alpha_2} \triangleq \mathbf{F}_{2D}^{(-\alpha_1, -\alpha_2)} \mathbf{x}_f^{\alpha_1, \alpha_2}. \quad (15)$$

B. Properties

The proposed 2D-GBFRFT inherits and extends several classical properties of FRFT and GFRFT. We summarize the main theoretical properties that establish its effectiveness in graph signal processing.

Property 1 (Identity): If $\alpha_1 = \alpha_2 = 0$, the 2D-GBFRFT reduces to the identity transform, i.e.,

$$\mathbf{F}_{2D}^{(0,0)} = \mathbf{F}_{G_2}^0 \otimes \mathbf{F}_{G_1}^0 = \mathbf{I}_{N_2} \otimes \mathbf{I}_{N_1} = \mathbf{I}_{N_1 N_2}. \quad (16)$$

Property 2 (Reduction to 2D-GFRFT): When $\alpha_1 = \alpha_2 = \alpha$, the 2D-GBFRFT reduces to the standard 2D-GFRFT:

$$\mathbf{F}_{2D}^{(\alpha, \alpha)} = \mathbf{F}_{G_2}^\alpha \otimes \mathbf{F}_{G_1}^\alpha = \mathbf{F}_{2D}^\alpha. \quad (17)$$

Property 3 (Unitarity): If both $\mathbf{F}_{G_1}^{\alpha_1}$ and $\mathbf{F}_{G_2}^{\alpha_2}$ are unitary, then $\mathbf{F}_{2D}^{(\alpha_1, \alpha_2)}$ is also unitary. Specifically,

$$\begin{aligned} (\mathbf{F}_{2D}^{(\alpha_1, \alpha_2)})^H \mathbf{F}_{2D}^{(\alpha_1, \alpha_2)} &= (\mathbf{F}_{G_2}^{\alpha_2} \otimes \mathbf{F}_{G_1}^{\alpha_1})^H (\mathbf{F}_{G_2}^{\alpha_2} \otimes \mathbf{F}_{G_1}^{\alpha_1}) \\ &= \left((\mathbf{F}_{G_2}^{\alpha_2})^H \mathbf{F}_{G_2}^{\alpha_2} \right) \otimes \left((\mathbf{F}_{G_1}^{\alpha_1})^H \mathbf{F}_{G_1}^{\alpha_1} \right) \\ &= \mathbf{I}_{N_1 N_2}, \end{aligned} \quad (18)$$

which establishes unitarity.

Property 4 (Index additivity): For any two sets of orders (α_1, α_2) and (β_1, β_2) , the additivity property holds:

$$\begin{aligned}
\mathbf{F}_{2D}^{(\alpha_1, \alpha_2)} \mathbf{F}_{2D}^{(\beta_1, \beta_2)} &= (\mathbf{F}_{G_2}^{\alpha_2} \otimes \mathbf{F}_{G_1}^{\alpha_1}) (\mathbf{F}_{G_2}^{\beta_2} \otimes \mathbf{F}_{G_1}^{\beta_1}) \\
&= (\mathbf{F}_{G_2}^{\alpha_2} \mathbf{F}_{G_2}^{\beta_2}) \otimes (\mathbf{F}_{G_1}^{\alpha_1} \mathbf{F}_{G_1}^{\beta_1}) \\
&= \mathbf{F}_{G_2}^{\alpha_2 + \beta_2} \otimes \mathbf{F}_{G_1}^{\alpha_1 + \beta_1} \\
&= \mathbf{F}_{2D}^{(\alpha_1 + \beta_1, \alpha_2 + \beta_2)}. \tag{19}
\end{aligned}$$

In particular, setting $(\beta_1, \beta_2) = (-\alpha_1, -\alpha_2)$ yields

$$\mathbf{F}_{2D}^{(\alpha_1, \alpha_2)} \mathbf{F}_{2D}^{(-\alpha_1, -\alpha_2)} = \mathbf{F}_{2D}^{(0,0)} = \mathbf{I}_{N_1 N_2}, \tag{20}$$

which confirms the invertibility of the 2D-GBFRFT.

IV. GEODESIC-COUPLED GRAPH FRACTIONAL FOURIER TRANSFORM

A. Definition

Following the Cartesian product setting introduced earlier, we consider a spatiotemporal signal $\mathbf{X} \in \mathbb{C}^{N_1 \times N_2}$ supported on $G_1 \square G_2$, where G_1 is the spatial factor and G_2 is the temporal factor. Let $\mathbf{F}_{G_1}^\alpha \in \mathbb{C}^{N_1 \times N_1}$ denote the spatial GFRFT of order $\alpha \in \mathbb{R}$ on G_1 . Along the temporal dimension, we consider two unitary fractional transforms of the same order $\beta \in \mathbb{R}$: a graph-induced temporal GFRFT $\mathbf{F}_{G_2}^\beta \in \mathbb{C}^{N_2 \times N_2}$ and a discrete FRFT matrix $\mathbf{F}^\beta \in \mathbb{C}^{N_2 \times N_2}$, satisfying

$$(\mathbf{F}_{G_2}^\beta)^H \mathbf{F}_{G_2}^\beta = \mathbf{I}_{N_2}, \quad (\mathbf{F}^\beta)^H \mathbf{F}^\beta = \mathbf{I}_{N_2}. \tag{21}$$

Although both operators are unitary, they generally yield different temporal spectral coordinates. As discussed in the motivation, a naive Euclidean interpolation between the two endpoints does not preserve unitarity in general. We therefore connect them through a unitary geodesic on the unitary group $U(N_2)$, constructed via the principal matrix logarithm and exponential.

Define the relative change-of-basis operator as

$$\mathbf{W}_t \triangleq (\mathbf{F}_{G_2}^\beta)^H \mathbf{F}^\beta \in \mathbb{C}^{N_2 \times N_2}. \tag{22}$$

Since both factors are unitary, \mathbf{W}_t is unitary, and all its eigenvalues lie on the unit circle.

Assumption 1 (Principal logarithm well-defined). We assume $-1 \notin \sigma(\mathbf{W}_t)$ so that the principal matrix logarithm $\log(\mathbf{W}_t)$ is well defined and unique.

Definition 4 (Temporal geodesic coupling). For $\lambda \in [0, 1]$, define

$$\mathbf{F}_{t,GC}^{(\lambda;\beta)} \triangleq \mathbf{F}_{G_2}^\beta \exp(\lambda \log(\mathbf{W}_t)). \tag{23}$$

This curve lies on $U(N_2)$ for all λ and admits a closed-form inverse.

Equivalent phase-domain form: Because \mathbf{W}_t is unitary, it admits an eigendecomposition

$$\mathbf{W}_t = \mathbf{S}_t \mathbf{\Lambda}_t \mathbf{S}_t^H, \quad \mathbf{\Lambda}_t = \text{diag}(e^{j\theta_1}, \dots, e^{j\theta_{N_2}}), \quad \theta_k \in (-\pi, \pi), \tag{24}$$

where \mathbf{S}_t is unitary and θ_k are principal phases. Substituting (24) into (23) yields

$$\mathbf{F}_{t,GC}^{(\lambda;\beta)} = \mathbf{F}_{G_2}^\beta \mathbf{S}_t \text{diag}(e^{j\lambda\theta_1}, \dots, e^{j\lambda\theta_{N_2}}) \mathbf{S}_t^H, \tag{25}$$

which makes explicit that λ linearly interpolates the eigenphases of \mathbf{W}_t . For a fixed β , when \mathbf{S}_t and $\{\theta_k\}_{k=1}^{N_2}$ are

computed once, (25) also enables efficient evaluation for multiple values of λ , since varying λ only updates the diagonal phase factors.

Definition 5 (GC-GFRFT). For $\mathbf{X} \in \mathbb{C}^{N_1 \times N_2}$, define the GC-GFRFT as

$$\mathbf{X}_{GC}^{(\lambda;\alpha,\beta)} = \mathbf{F}_{G_1}^\alpha \mathbf{X} (\mathbf{F}_{t,GC}^{(\lambda;\beta)})^T. \tag{26}$$

Equivalently, letting $\mathbf{x} \triangleq \text{vec}(\mathbf{X})$ and $\mathbf{x}_{GC}^{(\lambda;\alpha,\beta)} \triangleq \text{vec}(\mathbf{X}_{GC}^{(\lambda;\alpha,\beta)})$, the standard vec-Kronecker identity gives

$$\mathbf{x}_{GC}^{(\lambda;\alpha,\beta)} = \left(\mathbf{F}_{t,GC}^{(\lambda;\beta)} \otimes \mathbf{F}_{G_1}^\alpha \right) \mathbf{x} \triangleq \mathbf{F}_{GC}^{(\lambda;\alpha,\beta)} \mathbf{x}. \tag{27}$$

B. Properties

We next study the global GC operator

$$\mathbf{F}_{GC}^{(\lambda;\alpha,\beta)} \triangleq \mathbf{F}_{t,GC}^{(\lambda;\beta)} \otimes \mathbf{F}_{G_1}^\alpha \in \mathbb{C}^{(N_1 N_2) \times (N_1 N_2)}. \tag{28}$$

Unless otherwise stated, all results hold under Assumption 1 and the unitarity of $\mathbf{F}_{G_1}^\alpha$, $\mathbf{F}_{G_2}^\beta$, and \mathbf{F}^β .

Property 5 (Degeneracy to two endpoints). For $\lambda \in [0, 1]$, the GC operator degenerates to

$$\mathbf{F}_{GC}^{(0;\alpha,\beta)} = \mathbf{F}_{G_2}^\beta \otimes \mathbf{F}_{G_1}^\alpha, \quad \mathbf{F}_{GC}^{(1;\alpha,\beta)} = \mathbf{F}^\beta \otimes \mathbf{F}_{G_1}^\alpha. \tag{29}$$

Proof: See Appendix A.

Property 6 (Unitarity). For any $\lambda \in [0, 1]$,

$$(\mathbf{F}_{GC}^{(\lambda;\alpha,\beta)})^H \mathbf{F}_{GC}^{(\lambda;\alpha,\beta)} = \mathbf{I}_{N_1 N_2}. \tag{30}$$

Proof: See Appendix A.

Property 7 (Endpoint symmetry). Define the swapped-endpoint temporal coupling

$$\tilde{\mathbf{F}}_{t,GC}^{(\lambda;\beta)} \triangleq \mathbf{F}^\beta \exp\left(\lambda \log((\mathbf{F}^\beta)^H \mathbf{F}_{G_2}^\beta)\right), \tag{31}$$

and the corresponding global operator $\tilde{\mathbf{F}}_{GC}^{(\lambda;\alpha,\beta)} \triangleq \tilde{\mathbf{F}}_{t,GC}^{(\lambda;\beta)} \otimes \mathbf{F}_{G_1}^\alpha$. Then, for all $\lambda \in [0, 1]$,

$$\tilde{\mathbf{F}}_{GC}^{(\lambda;\alpha,\beta)} = \mathbf{F}_{GC}^{(1-\lambda;\alpha,\beta)}. \tag{32}$$

Proof: See Appendix A.

V. LEARNABLE WIENER FILTERING IN FRACTIONAL SPECTRAL DOMAINS

We extend the Wiener filtering principle to spatiotemporal graph signals under the proposed GC-GFRFT framework. Consider the stochastic observation model over a space-time domain

$$\mathbf{Y} = \mathbf{G}_S \mathbf{X} \mathbf{G}_T + \mathbf{N}, \tag{33}$$

where $\mathbf{G}_S \in \mathbb{C}^{N_1 \times N_1}$ and $\mathbf{G}_T \in \mathbb{C}^{N_2 \times N_2}$ denote known linear system responses associated with the spatial graph G_1 and the temporal dimension, respectively. The matrix $\mathbf{X} \in \mathbb{C}^{N_1 \times N_2}$ represents the stochastic space-time signal, and \mathbf{N} denotes additive noise. Letting $\mathbf{x} = \text{vec}(\mathbf{X})$ and $\mathbf{n} = \text{vec}(\mathbf{N})$, the model can be written in vectorized form as

$$\mathbf{y} = (\mathbf{G}_T^T \otimes \mathbf{G}_S) \mathbf{x} + \mathbf{n}. \tag{34}$$

When $\lambda = 0$, the temporal GC basis reduces to the graph-induced temporal fractional basis, and the resulting transform specializes to the decoupled 2D-GBFRFT with independent spatial and temporal orders.

A. Learnable Spectral Filtering via Gradient Descent

A direct grid search over fractional orders incurs exponentially many configurations as the number of tunable parameters increases. To avoid this, we leverage the differentiability of the GC-GFRFT operator and jointly optimize the fractional orders and diagonal spectral filter coefficients via gradient-based learning.

Specifically, the fractional orders (α, β) are treated as learnable parameters, whereas the coupling parameter λ is treated as a fixed structural hyperparameter that controls the geodesic coupling between the graph-induced temporal basis and the discrete temporal basis. In practice, λ is selected by a coarse search with step size 0.1 and then kept fixed during optimization; hence, λ is excluded from gradient updates.

Theorem 1 (Differentiability of GC-GFRFT with Respect to Fractional Orders): Let $\mathbf{F}_{\text{GC}}^{(\lambda; \alpha, \beta)}$ denote the GC-GFRFT operator defined in (27). For any fixed λ satisfying Assumption 1, $\mathbf{F}_{\text{GC}}^{(\lambda; \alpha, \beta)}$ is differentiable with respect to α and β . This differentiability enables the following risk-minimization formulation:

$$\begin{aligned} \min_{\alpha, \beta, \mathbf{h}} \mathcal{L}(\alpha, \beta, \mathbf{h}; \lambda) \\ = \mathbb{E} \left\{ \left\| \left(\mathbf{F}_{\text{GC}}^{(\lambda; \alpha, \beta)} \right)^{-1} \mathbf{H}_{\text{GC}} \mathbf{F}_{\text{GC}}^{(\lambda; \alpha, \beta)} \mathbf{y} - \mathbf{x} \right\|_2^2 \right\} \end{aligned} \quad (35)$$

where $\mathbf{H}_{\text{GC}} = \text{diag}(\mathbf{h})$ is the diagonal spectral filter in the GC-GFRFT domain. In implementation, the diagonal filtering corresponds to an element-wise multiplication in the matrix spectral domain, and (35) is evaluated via (26) without explicitly forming $\mathbf{F}_{\text{GC}}^{(\lambda; \alpha, \beta)}$.

The corresponding gradient-descent updates are given by

$$\begin{bmatrix} \alpha^{(k+1)} \\ \beta^{(k+1)} \end{bmatrix} = \begin{bmatrix} \alpha^{(k)} \\ \beta^{(k)} \end{bmatrix} - \gamma \begin{bmatrix} \frac{\partial \mathcal{L}}{\partial \alpha} \\ \frac{\partial \mathcal{L}}{\partial \beta} \end{bmatrix}, \quad \mathbf{h}^{(k+1)} = \mathbf{h}^{(k)} - \gamma_h \frac{\partial \mathcal{L}}{\partial \mathbf{h}}. \quad (36)$$

Here, γ and γ_h denote the learning rates. Since the forward map in (35) consists of differentiable matrix functions and linear operators, the gradients are well-defined.

Proof: See Appendix B.

The overall procedure is summarized in Algorithm 1.

B. Computational Efficiency and Optimization Analysis

This subsection analyzes the computational cost and optimization behavior of the proposed learnable Wiener filtering framework. The efficiency primarily stems from the separable implementation of the GC-GFRFT in (26), which avoids explicitly forming the $(N_1 N_2) \times (N_1 N_2)$ Kronecker matrix. In addition, the phase-domain representation in (25) clarifies how the fixed coupling parameter λ enters the temporal operator through diagonal phase factors.

The overall computation consists of an offline spectral preprocessing stage and an online iterative learning stage. In the dense setting, preprocessing computes the eigendecompositions required by the spatial and temporal graph-induced fractional bases, incurring a one-time cost of $O(N_1^3 + N_2^3)$ because the underlying graph topologies are fixed. These decompositions provide fixed eigenvector bases; during training, changing α or β only updates the associated diagonal phase

Algorithm 1 GC-GFRFT Order and Filter Optimization

Require: Observation \mathbf{Y} , fixed coupling parameter λ , learning rates γ, γ_h , iterations L

Ensure: Learned orders (α, β) and diagonal filter \mathbf{H}_{GC}

- 1: Initialize $\alpha = 0.5$, $\beta = 0.5$, and $\mathbf{H}_{\text{GC}} = \mathbf{I}$
 - 2: **for** $k = 1$ to L **do**
 - 3: Construct spatial basis $\mathbf{F}_{G_1}^\alpha$ and temporal coupling basis $\mathbf{F}_{t, \text{GC}}^{(\lambda; \beta)}$ via (23)
 - 4: Compute the GC spectral representation: $\hat{\mathbf{Y}} = \mathbf{F}_{G_1}^\alpha \mathbf{Y} (\mathbf{F}_{t, \text{GC}}^{(\lambda; \beta)})^\top$
 - 5: Apply element-wise spectral filtering: $\hat{\mathbf{X}}_{\text{spec}} = \mathbf{H}_{\text{GC}}^{\text{mat}} \circ \hat{\mathbf{Y}}$
 - 6: Inverse transform: $\hat{\mathbf{X}} = (\mathbf{F}_{G_1}^\alpha)^H \hat{\mathbf{X}}_{\text{spec}} (\mathbf{F}_{t, \text{GC}}^{(\lambda; \beta)})^*$
 - 7: Evaluate the empirical loss corresponding to (35)
 - 8: Update $(\alpha, \beta, \mathbf{h})$ according to (36)
 - 9: **end for**
 - 10: **return** (α, β) and \mathbf{H}_{GC}
-

factors. Hence, the transform application reuses the cached eigenvectors and evaluates the operator via products of the form $\mathbf{V} \text{diag}(\cdot) \mathbf{V}^H$, *without recomputing eigendecompositions across epochs.*

During learning, the forward and inverse GC-GFRFT evaluations are computed efficiently through sequential matrix multiplications in (26). For $\mathbf{X} \in \mathbb{C}^{N_1 \times N_2}$, each forward or inverse pass consists of one left multiplication by $\mathbf{F}_{G_1}^\alpha$ and one right multiplication by $(\mathbf{F}_{t, \text{GC}}^{(\lambda; \beta)})^\top$. With dense arithmetic, each transform evaluation costs $O(N_1^2 N_2 + N_1 N_2^2)$. The diagonal spectral filter $\mathbf{H}_{\text{GC}} = \text{diag}(\mathbf{h})$ is applied element-wise in the spectral domain and requires only $O(N_1 N_2)$ operations. Consequently, the per-epoch complexity is dominated by a constant number of forward/inverse transform evaluations.

For the temporal coupling operator, (25) shows that for a fixed β , the dependence on λ is confined to diagonal phase factors. However, since β is learnable, $\mathbf{W}_t(\beta)$ changes across epochs. Updating $\mathbf{F}_{t, \text{GC}}^{(\lambda; \beta)}$ via (25) requires recomputing a spectral factorization of the $N_2 \times N_2$ unitary matrix $\mathbf{W}_t(\beta)$, which has a dense worst-case cost of $O(N_2^3)$. In typical spatiotemporal settings where $N_2 \ll N_1$, this term is substantially smaller than the spatial transform cost $O(N_1^2 N_2)$ and therefore does not change the overall scaling. Table I summarizes the parameter counts and computational complexities of all considered transforms.

The learning objective exhibits a hybrid structure. For fixed (α, β, λ) , optimizing the diagonal spectral filter coefficients \mathbf{h} reduces to a convex quadratic problem. Optimizing the fractional orders (α, β) is generally non-convex because the GC-GFRFT operators depend nonlinearly on these parameters; accordingly, first-order methods converge to stationary points in general. In our experiments, the proposed operator family is differentiable with respect to (α, β) , and standard optimizers exhibit stable convergence under the initialization described in Algorithm 1.

TABLE I
COMPARISON OF LEARNABLE PARAMETERS AND COMPUTATIONAL
COMPLEXITY AMONG DIFFERENT FRACTIONAL TRANSFORMS

Method	Learnable Parameters	Asymptotic Complexity
2D-GFRFT	$N_1 N_2 + 1$	$O(N_1^3 + N_2^3 + L(N_1^2 N_2 + N_1 N_2^2))$
2D-GBFRFT	$N_1 N_2 + 2$	$O(N_1^3 + N_2^3 + L(N_1^2 N_2 + N_1 N_2^2))$
JFRFT	$N_1 N_2 + 2$	$O(N_1^3 + N_2^3 + L(N_1^2 N_2 + N_1 N_2^2))$
GC-GFRFT	$N_1 N_2 + 2$	$O(N_1^3 + N_2^3 + L(N_1^2 N_2 + N_1 N_2^2 + N_2^3))$

Note: N_1 and N_2 denote the sizes of the spatial and temporal graphs, and L is the number of training epochs. The term $O(N_1^3 + N_2^3)$ accounts for one-time offline eigendecompositions for graph-induced bases. For transforms involving a DFRFT temporal basis (e.g., JFRFT), the temporal basis can be precomputed once; we report a dense upper bound for consistency, while faster constructions may reduce this cost. The online cost is dominated by separable transform evaluations. For GC-GFRFT, when β is learnable, updating $\mathbf{F}_{t,GC}^{(\lambda;\beta)}$ requires recomputing a spectral factorization of $\mathbf{W}_t(\beta)$, introducing an additional $O(N_2^3)$ term per epoch. The coupling parameter λ is treated as a fixed structural hyperparameter and is not counted as learnable.

VI. APPLICATIONS ON REAL-WORLD DATA

A. Denoising of Time-Varying Graph Signals

In [1], time-varying graph signals are modeled by representing the temporal dimension as a path graph and the spatial relationships by another graph, thereby forming a Cartesian product graph. This spatiotemporal modeling protocol enables a direct comparison with JFRFT under the same data and graph-construction setting. To evaluate denoising performance, we apply our framework to three real-world spatiotemporal datasets adopted from the benchmark setting in [42], namely COVID-19, Sea surface temperature (SST), and PM-25 air quality. For each dataset, the spatial relationships are modeled by k -nearest neighbor graphs, abbreviated as k -NN, with $k \in \{3, 4, 5\}$, and corrupted observations are generated by injecting additive white Gaussian noise (AWGN) with standard deviation $\sigma \in \{0.6, 0.9, 1.2\}$ into the clean spatiotemporal signals.

To ensure a principled comparison within the class of fractional transform-based approaches, we employ the same GD optimization protocol for 2D-GFRFT, 2D-GBFRFT, JFRFT, and the proposed GC-GFRFT. Specifically, the learning rate is set to 0.1 and the number of iterations is fixed to 200. All fractional orders are initialized to 0.5, and the diagonal spectral filter is initialized as the identity matrix. This unified setup isolates the effect of the underlying fractional spectral representations from confounding factors arising from heterogeneous optimization choices.

For GC-GFRFT, the coupling regularization parameter λ is selected via an outer grid search with step size 0.1 and then kept fixed during optimization. Thus, λ is excluded from the learnable-parameter count and is not updated by gradient-based learning. For each candidate λ , the remaining fractional orders and the diagonal filter are optimized using the same GD protocol described above, and the reported results correspond to the best-performing λ under the adopted validation criterion.

As reported in Tables II–IV, 2D-GBFRFT improves upon 2D-GFRFT in most settings, which supports the advantage of decoupling fractional orders across spatial and temporal dimensions. A small number of configurations exhibit inferior performance, which is consistent with the nonconvexity

induced by fractional spectral parameterization and the sensitivity of first-order optimization to initialization and local stationary points. Moreover, the relative ordering between 2D-GBFRFT and JFRFT varies across datasets and graph constructions, indicating that no single fixed fractional basis is uniformly optimal for real-world time-varying graph signals.

Relative to classical filtering baselines, including the spectral graph wavelet transform (SGWT) [18], median filtering [60], and autoregressive moving-average (ARMA) graph filtering [24], fractional transform-based methods achieve substantially lower MSE across nearly all noise levels and k -NN settings. These results suggest that adaptive fractional spectral representations provide a stronger denoising prior than hand-crafted smoothing operators.

Finally, GC-GFRFT attains the best or tied-best performance in the majority of configurations, demonstrating robust effectiveness across heterogeneous spatiotemporal characteristics. We further compare GC-GFRFT with representative graph neural network baselines, including the graph convolutional network (GCN) [61], the graph attention network (GAT) [62], and Chebyshev graph convolution (ChebyNet) [63]. Since neural models are commonly trained under model-specific practices such as learning-rate schedules, numbers of epochs, and early-stopping criteria, these baselines are reported under their standard training and model-selection protocols rather than being constrained to the GD setup adopted for fractional transforms. Under these typical settings, GC-GFRFT remains highly competitive and often yields lower MSE; however, in a limited number of configurations, a neural baseline can achieve slightly better performance. Overall, the results demonstrate that GC-GFRFT consistently surpasses classical filtering baselines while providing performance that is superior or comparable to representative neural approaches on real-world time-varying graph signals.

B. Deblurring of Dynamic Images

We further evaluate the proposed GC-GFRFT on dynamic image deblurring and compare it with fractional transform baselines, including 2D-GFRFT, 2D-GBFRFT, and JFRFT. In addition, we report results of three representative learning-based deblurring methods, DeepDeblur [64], Restormer [65], and NAFNet [66], as external baselines. Experiments are conducted on the REDS dataset. We extract three consecutive frames, resize them to 200×200 pixels, and partition each frame into 100 non-overlapping patches of size 20×20 . Each triplet of corresponding patches across the three frames is modeled as a spatiotemporal graph signal, where grayscale intensities are treated as signal values. The spatial graph is constructed as a 4-nearest neighbor graph based on pixel locations, and the temporal dimension is represented by a 3-node path graph.

Each 20×20 patch triplet is treated as an independent instance for optimization. The fractional orders and diagonal filter coefficients are optimized in a patch-wise manner, and the restored patches are reassembled to reconstruct the deblurred sequence. Adaptive filtering is performed under the respective transforms (2D-GFRFT, 2D-GBFRFT, JFRFT, and

TABLE II
DENOISING RESULTS (MSE) ON THE COVID-19 DATASET

Method	3-NN			4-NN			5-NN		
	$\sigma=0.6$	$\sigma=0.9$	$\sigma=1.2$	$\sigma=0.6$	$\sigma=0.9$	$\sigma=1.2$	$\sigma=0.6$	$\sigma=0.9$	$\sigma=1.2$
Fractional Transform-Based Methods									
2D-GFRFT	0.6424	1.0626	1.0749	0.4901	0.8104	1.1075	0.3828	0.5896	0.7687
(α)	(0.307)	(-0.263)	(-0.485)	(0.285)	(0.298)	(0.788)	(0.682)	(0.860)	(1.184)
2D-GBFRFT	0.1060	0.2155	0.3459	0.4012	0.6977	1.1212	0.1077	0.2216	0.3593
(α_1, α_2)	(0.033, 0.999)	(0.047, 0.998)	(0.060, 0.998)	(1.358, 0.594)	(1.362, 0.566)	(2.129, 0.565)	(0.008, 1.000)	(0.005, 1.000)	(-0.002, 1.000)
JFRFT	0.1051	0.2164	0.7659	0.4095	0.7371	0.3538	0.7058	1.1149	0.3693
(α, β)	(0.051, 0.996)	(0.072, 0.995)	(1.055, 1.082)	(1.281, 0.609)	(1.274, 0.611)	(0.057, 1.000)	(0.547, 0.318)	(0.553, 0.281)	(-0.040, 1.000)
GC-GFRFT	0.1051	0.2155	0.3459	0.1697	0.2740	0.3538	0.1077	0.2216	0.3593
(α, β, λ)	(0.051, 0.996, 1.000)	(0.047, 0.998, 0.000)	(0.060, 0.998, 0.000)	(0.060, 0.715, 0.800)	(0.071, 1.019, 0.800)	(0.057, 1.000, 1.000)	(0.008, 1.000, 0.000)	(0.005, 1.000, 0.000)	(-0.002, 1.000, 0.000)
Traditional Baselines									
SGWT	3.5500	6.8600	11.5600	3.5200	6.8400	11.5600	3.5000	6.7900	11.5100
Median	4.5300	9.5900	17.2800	5.2500	9.9700	16.5400	4.5700	9.0500	14.9300
ARMA	2.4300	3.3200	4.2100	2.4300	2.9800	3.4900	2.3100	2.7200	3.1000
Graph Neural Network Baselines									
GCN	1.2613	1.3116	1.3455	1.3972	1.4315	1.4547	1.4741	1.5060	1.5163
GAT	1.3306	1.2610	1.2498	1.3729	1.4338	1.5736	1.4473	1.4668	1.5487
ChebyNet	0.9834	1.1955	1.3489	0.7331	0.9758	1.1557	0.4505	0.5852	0.6853

TABLE III
DENOISING RESULTS (MSE) ON THE SST DATASET

Method	3-NN			4-NN			5-NN		
	$\sigma=0.6$	$\sigma=0.9$	$\sigma=1.2$	$\sigma=0.6$	$\sigma=0.9$	$\sigma=1.2$	$\sigma=0.6$	$\sigma=0.9$	$\sigma=1.2$
Fractional Transform-Based Methods									
2D-GFRFT	0.7200	1.5089	2.4722	0.7888	1.6653	2.7415	0.6310	1.2809	2.0307
(α)	(0.698)	(0.684)	(0.668)	(0.262)	(0.262)	(0.265)	(0.783)	(0.792)	(0.820)
2D-GBFRFT	0.6534	1.3608	2.2075	0.5552	1.0648	1.7662	0.6064	1.2161	1.9799
(α_1, α_2)	(0.582, 0.740)	(0.561, 0.755)	(0.522, 0.774)	(0.181, 0.827)	(0.163, 1.003)	(0.165, 1.000)	(0.739, 0.379)	(0.753, 0.484)	(0.762, 0.517)
JFRFT	1.1685	2.2851	3.4158	2.1764	1.1908	2.0045	0.4772	0.8394	1.4031
(α, β)	(0.752, 0.747)	(0.748, 0.779)	(0.850, 0.889)	(0.430, 0.447)	(0.185, 0.994)	(0.185, 1.000)	(0.740, 0.642)	(0.667, 0.759)	(0.669, 0.744)
GC-GFRFT	0.6395	1.3608	2.2075	0.5295	1.0648	1.2807	0.4772	0.8394	1.4031
(α, β, λ)	(0.604, 0.717, 0.100)	(0.561, 0.755, 0.000)	(0.522, 0.774, 0.000)	(0.238, 1.238, 0.400)	(0.163, 1.003, 0.000)	(1.098, 1.289, 0.600)	(0.740, 0.642, 1.000)	(0.667, 0.759, 1.000)	(0.669, 0.744, 1.000)
Traditional Baselines									
SGWT	5.3200	10.7100	18.2900	5.3000	10.6200	18.1200	4.8400	9.7700	16.7800
Median	6.0400	13.7600	24.2800	6.3400	12.6900	21.6500	5.4000	10.0900	16.8300
ARMA	2.9700	4.3900	5.7900	3.2400	4.3500	5.2800	3.7300	4.7800	5.6300
Graph Neural Network Baselines									
GCN	2.5521	3.6928	4.4128	1.9366	2.6767	3.3740	2.1656	2.9620	3.7989
GAT	2.5520	3.7652	4.9559	3.0085	4.2111	5.4557	3.2268	4.5049	5.9509
ChebyNet	3.4350	4.7864	5.4158	3.0030	4.3172	5.3172	2.6764	4.0671	4.8447

TABLE IV
DENOISING RESULTS (MSE) ON THE PM-25 DATASET

Method	3-NN			4-NN			5-NN		
	$\sigma=0.6$	$\sigma=0.9$	$\sigma=1.2$	$\sigma=0.6$	$\sigma=0.9$	$\sigma=1.2$	$\sigma=0.6$	$\sigma=0.9$	$\sigma=1.2$
Fractional Transform-Based Methods									
2D-GFRFT	0.6636	1.2474	1.8847	0.9222	1.7594	2.1018	0.6605	1.1877	1.7555
(α)	(0.813)	(0.804)	(0.801)	(0.584)	(0.577)	(1.014)	(0.315)	(0.318)	(0.320)
2D-GBFRFT	0.6398	1.1952	1.8206	0.7653	1.5059	2.2999	0.6008	1.1854	1.7549
(α_1, α_2)	(0.784, 1.371)	(0.723, 0.513)	(0.716, 0.507)	(0.613, -0.273)	(0.618, 0.272)	(0.624, 0.275)	(0.474, 0.527)	(0.322, 0.298)	(0.322, 0.311)
JFRFT	0.4872	0.8825	1.3697	0.4219	0.8629	1.3931	0.4497	0.9242	1.4784
(α, β)	(0.785, 0.517)	(0.846, 0.573)	(0.827, 0.563)	(0.965, 0.561)	(0.977, 0.567)	(0.974, 0.564)	(0.480, 0.541)	(0.490, 0.538)	(0.505, 0.536)
GC-GFRFT	0.3746	0.7509	1.1665	0.4219	0.8629	1.3445	0.4191	0.8275	1.3906
(α, β, λ)	(0.857, 0.868, 0.700)	(0.852, 0.855, 0.700)	(0.701, 1.398, 0.300)	(0.965, 0.561, 1.000)	(0.977, 0.567, 1.000)	(1.025, 0.944, 0.600)	(0.418, 0.656, 0.600)	(1.078, 1.475, 0.300)	(0.414, 0.686, 0.600)
Traditional Baselines									
SGWT	3.6100	6.6500	10.9800	3.3700	6.1900	10.2300	3.3700	6.2000	10.2400
Median	5.0300	8.9600	14.7000	4.3800	7.4200	11.8700	4.6700	7.7800	12.0500
ARMA	2.6200	3.3000	3.9700	2.5000	3.0300	3.5900	2.4000	2.7500	3.0800
Graph Neural Network Baselines									
GCN	0.7009	0.7143	0.6977	0.7127	0.7210	0.7150	0.7032	0.7084	0.6992
GAT	0.8098	0.7671	0.7785	0.8110	0.7697	0.7958	0.7495	0.7194	0.7359
ChebyNet	0.6436	0.6625	0.6766	0.5952	0.6204	0.6527	0.6026	0.6215	0.6459

GC-GFRFT), with MSE used as the optimization objective. Optimization is carried out using Adam with a learning rate of 2×10^{-2} for 100 epochs. The fractional orders are initialized to 0.8, and the diagonal filter is initialized as the identity matrix.

For GC-GFRFT, the coupling parameter λ is selected by an outer grid search with step size 0.1 and is kept fixed during the subsequent optimization. Gradient-based updates are applied only to the fractional orders and the diagonal spectral filter coefficients; in particular, λ is not updated by backpropagation

and is not counted as a learnable parameter.

For each frame t , we compute MSE, peak signal-to-noise ratio (PSNR), and structural similarity index measure (SSIM) as follows:

$$MSE_t = \frac{1}{HW} \sum_{i,j} \left(I_t(i,j) - \hat{I}_t(i,j) \right)^2, \quad (37)$$

$$PSNR_t = 10 \log_{10} \left(\frac{\text{MAX}^2}{MSE_t} \right), \quad (38)$$

$$SSIM_t = \frac{(2\mu_{I_t}\mu_{\hat{I}_t} + C_1)(2\sigma_{I_t\hat{I}_t} + C_2)}{(\mu_{I_t}^2 + \mu_{\hat{I}_t}^2 + C_1)(\sigma_{I_t}^2 + \sigma_{\hat{I}_t}^2 + C_2)}, \quad (39)$$

where I_t and \hat{I}_t denote the ground-truth and reconstructed frames at time t , respectively, and H and W are the image height and width.

Quantitative results are reported in Tables V and VI. Among the fractional transform baselines, 2D-GBFRFT consistently improves upon 2D-GFRFT, supporting the benefit of allowing distinct fractional orders along the spatial and temporal dimensions. GC-GFRFT further reduces MSE_{avg} and achieves the best overall performance in terms of MSE_{avg} , $PSNR_{avg}$, and $SSIM_{avg}$, indicating that coupling-aware fractional modeling provides a more effective transform-domain representation for dynamic deblurring under patch-wise optimization.

For the fractional transform-based methods, we adopt an identical patch-wise instance-adaptive optimization protocol, where the fractional orders and diagonal spectral filter are updated by Adam for each patch triplet. In contrast, the learning-based baselines are evaluated in inference mode using their official implementations and publicly released weights, without any test-time parameter adaptation. Therefore, comparisons with learning-based methods primarily reflect the effectiveness of instance-adaptive fractional spectral modeling under short temporal windows, rather than a fully matched training paradigm.

Fig. 2 provides qualitative comparisons for dynamic image deblurring. For each frame, a representative region is highlighted on the full image, and the corresponding magnified patch is shown beneath it. Compared with the competing methods, GC-GFRFT recovers sharper edges and clearer local textures, while exhibiting fewer residual blur artifacts around object boundaries and fine structures. These visual observations are consistent with the quantitative results and further demonstrate the effectiveness of GC-GFRFT for dynamic image deblurring.

C. Denoising of Dynamic Images

To further evaluate robustness beyond dynamic deblurring, we consider a dynamic image denoising task on the REDS dataset. Clean sequences are first converted to floating-point representations and normalized to the range $[0, 1]$. Additive white Gaussian noise (AWGN) with zero mean and standard deviation $\sigma/255$ is then injected into the normalized intensities, where we set $\sigma = 18$ on the 8-bit scale. After noise injection, the corrupted frames are clipped to the valid range $[0, 1]$ and re-quantized to 8-bit integers, which follows a standard digital imaging pipeline and ensures valid pixel representations.

We compare the proposed GC-GFRFT with fractional transform baselines, including 2D-GFRFT, 2D-GBFRFT, and JFRFT. We also include three classical spatial denoisers as reference baselines, namely Gaussian filtering, median filtering, and non-local means (NLM), following the implementation and parameter settings in [43]. These classical methods are applied frame-wise without any learning or test-time adaptation. Gaussian filtering uses a 5×5 kernel with the standard deviation determined by the kernel size. Median filtering uses a

TABLE V
COMPARISON OF DEBLURRING PERFORMANCE (MSE/PSNR/SSIM) ON THE REDS DATASET

Dataset	Method	Frame	MSE	PSNR	SSIM
REDS	2D-GFRFT	Frame 1	1.0389	47.96	0.9992
		Frame 2	0.9281	48.45	0.9992
		Frame 3	1.2405	47.20	0.9991
	2D-GBFRFT	Frame 1	1.0010	48.13	0.9993
		Frame 2	0.9137	48.52	0.9993
		Frame 3	1.2424	47.19	0.9992
	JFRFT	Frame 1	0.9406	48.40	0.9994
		Frame 2	0.9392	48.40	0.9993
		Frame 3	1.2460	47.18	0.9991
	GC-GFRFT	Frame 1	0.9564	48.32	0.9994
		Frame 2	0.9308	48.44	0.9993
		Frame 3	1.2107	47.30	0.9992
	DeepDeblur	Frame 1	204.6643	25.02	0.8140
		Frame 2	214.1956	24.82	0.8054
		Frame 3	229.0492	24.53	0.8028
Restormer	Frame 1	253.9732	24.08	0.7949	
	Frame 2	245.9362	24.22	0.7961	
	Frame 3	262.5448	23.94	0.7934	
NAFNet	Frame 1	245.4231	24.23	0.7994	
	Frame 2	238.4010	24.36	0.7997	
	Frame 3	266.5690	23.87	0.7901	

TABLE VI
DEBLURRING PERFORMANCE IN TERMS OF MSE_{avg} , $PSNR_{avg}$, AND $SSIM_{avg}$ ON THE REDS DATASET

Dataset	Method	MSE_{avg}	$PSNR_{avg}$	$SSIM_{avg}$
REDS	2D-GFRFT	1.0692	47.87	0.9992
	2D-GBFRFT	1.0524	47.95	0.9992
	JFRFT	1.0419	47.99	0.9993
	GC-GFRFT	1.0326	48.02	0.9993
	DeepDeblur	215.9697	24.79	0.8074
	Restormer	254.1514	24.08	0.7948
	NAFNet	250.1310	24.15	0.7964

5×5 neighborhood. NLM denoising uses filter strength $h = 20$ with a 7×7 template window and a 21×21 search window. For the fractional transform-based methods, all experimental settings—including the patch-wise spatiotemporal graph construction, initialization strategy, optimization hyperparameters, and stopping criterion—are kept identical to those used in the preceding dynamic deblurring experiments unless otherwise specified, thereby ensuring a consistent and fair comparison within the fractional transform family.

Quantitative results are reported in Tables VII and VIII. Overall, the fractional transform-based methods consistently outperform classical spatial filters across the evaluated frames. This indicates that exploiting spatiotemporal structure through graph-based spectral representations provides a stronger denoising prior than purely spatial neighborhood smoothing. Within the fractional transform family, decoupling the fractional orders along the spatial and temporal dimensions generally improves over using a single shared order, consistent with the benefit of increased modeling flexibility. The proposed GC-GFRFT achieves the best overall average performance and

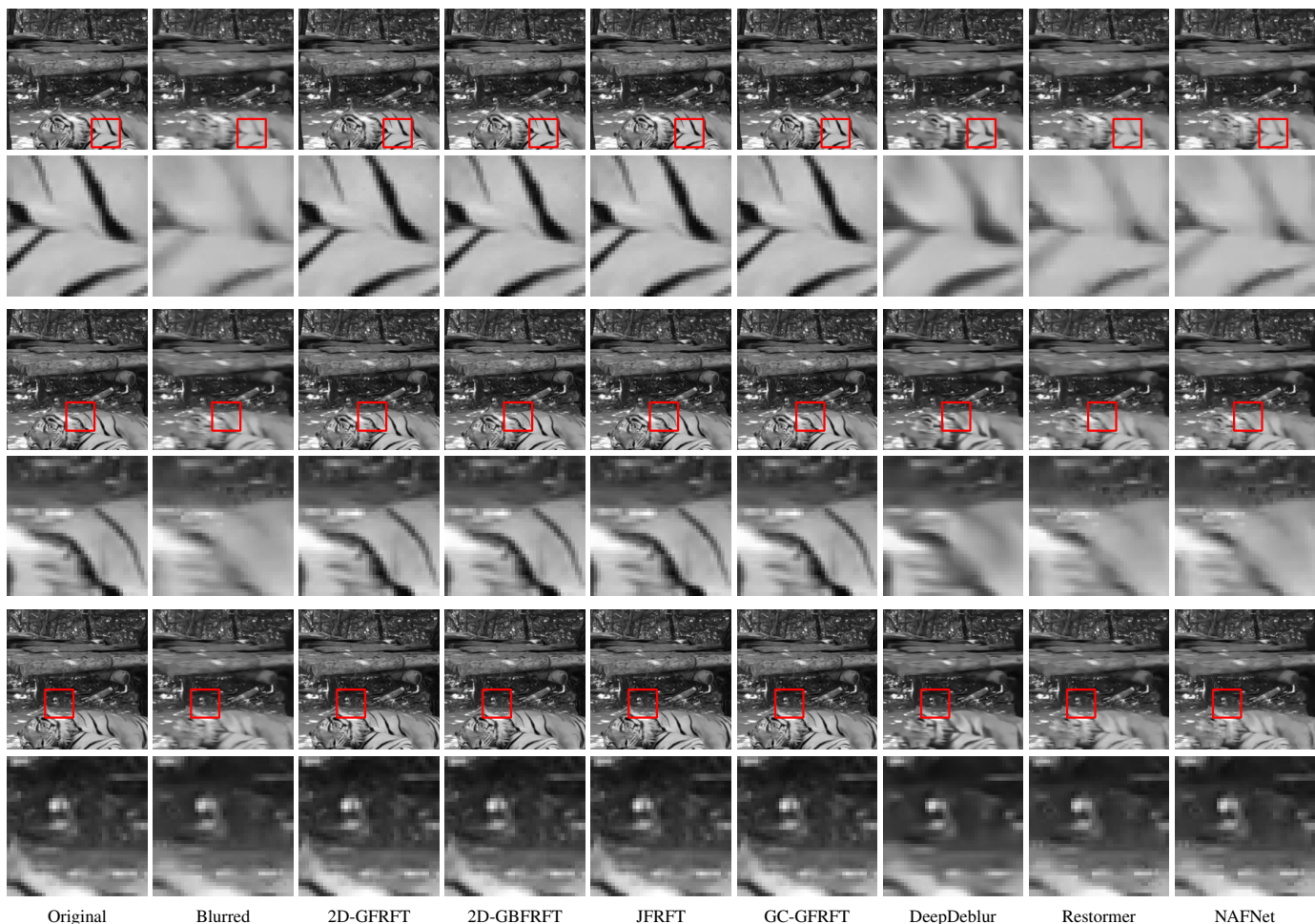


Fig. 2. Visual comparison on the REDS sequence for dynamic image deblurring. For each frame, the first row shows the selected region on the full, and the second row shows the corresponding magnified patch.

remains highly competitive at the per-frame level, supporting the effectiveness of coupling-aware fractional modeling for dynamic denoising.

Fig. 3 provides qualitative comparisons for dynamic image denoising. For each frame, a representative region is highlighted on the full image, and the corresponding magnified patch is shown beneath it. Compared with classical spatial filters, the fractional transform-based methods preserve more meaningful local structures while suppressing noise more effectively. Among them, GC-GFRFT produces cleaner textures and fewer residual noise artifacts, while avoiding the oversmoothing effects observed in Gaussian filtering, median filtering, and NLM. These observations are consistent with the quantitative results in Tables VII and VIII, further supporting the effectiveness of GC-GFRFT for dynamic image denoising.

VII. CONCLUSION AND FUTURE WORK

In this paper, we developed a unified fractional spectral framework for graph signals on Cartesian product graphs, extending conventional integer-order and single-parameter fractional transforms. We first proposed the 2D-GBFRFT, which assigns independent fractional orders to the factor graphs and relaxes the shared-order constraint of the standard 2D-GFRFT,

thereby improving modeling flexibility for spatiotemporal signals. To bridge the graph-induced temporal basis and the discrete temporal basis, we further introduced the GC-GFRFT by constructing a coupling path on the unitary manifold. This construction preserves unitarity and admits a closed-form inverse, providing a principled link between connectivity-induced graph spectra and classical temporal spectral representations.

Building upon these transforms, we formulated a differentiable Wiener filtering approach in which the fractional orders are optimized end-to-end via gradient-based learning, while the coupling parameter serves as a fixed structural regularizer. Experiments on real-world tasks, including time-varying graph-signal denoising and dynamic image restoration, demonstrate consistent gains over existing fractional transforms and remain competitive with representative learning-based baselines.

Despite these promising results, the current framework still has several limitations. In particular, the proposed GC-GFRFT is presently restricted to interpolation between two endpoint unitary bases and therefore does not yet support more general spectral extrapolation. In addition, the coupling parameter λ is treated as a fixed structural hyperparameter rather than being jointly learned with the remaining model parameters.

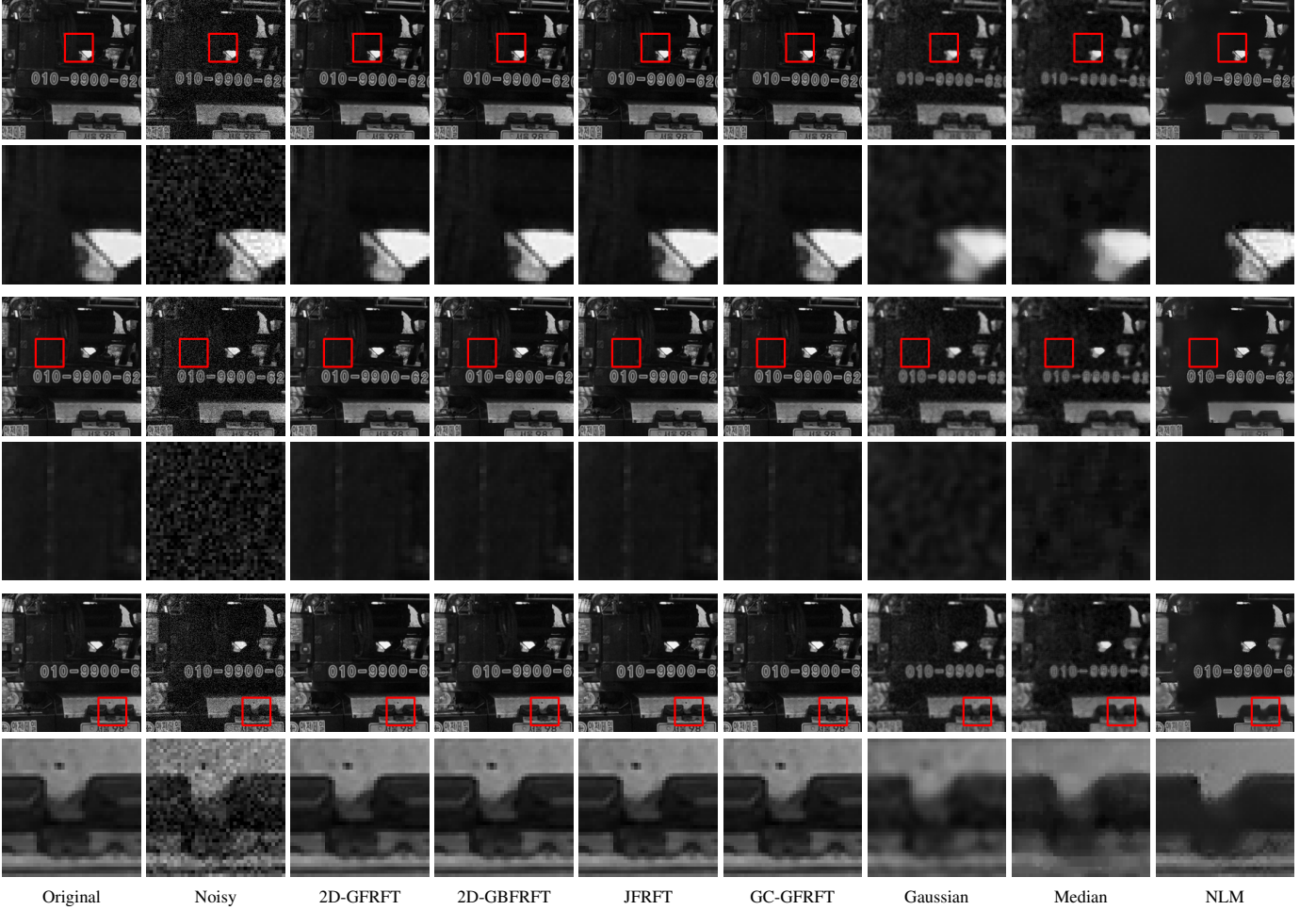


Fig. 3. Visual comparison on the REDS sequence for dynamic image denoising. For each frame, the first row shows the selected region on the full image, and the second row shows the corresponding magnified patch.

Future work will therefore focus on extending the geodesic coupling mechanism beyond the current interpolation range to support spectral extrapolation. Another important direction is to integrate differentiable GC-GFRFT modules into deep graph neural networks as lightweight spectral layers, thereby enhancing spectral expressiveness with modest parameter overhead.

APPENDIX A

PROOF OF PROPERTIES 5–7

Proof of Property 5: From (23), $\mathbf{F}_{t,GC}^{(0;\beta)} = \mathbf{F}_{G_2}^\beta$. At $\lambda = 1$, Assumption 1 gives $\exp(\log(\mathbf{W}_t)) = \mathbf{W}_t$, hence

$$\mathbf{F}_{t,GC}^{(1;\beta)} = \mathbf{F}_{G_2}^\beta \mathbf{W}_t = \mathbf{F}_{G_2}^\beta (\mathbf{F}_{G_2}^\beta)^\mathbf{H} \mathbf{F}^\beta = \mathbf{F}^\beta.$$

Substituting into (28) yields (29). \blacksquare

Proof of Property 6: Let $\mathbf{A} \triangleq \log(\mathbf{W}_t)$. Under Assumption 1, $\mathbf{A}^\mathbf{H} = -\mathbf{A}$, so $\exp(\lambda \mathbf{A})$ is unitary for any real λ , and in particular for $\lambda \in [0, 1]$. Thus $\mathbf{F}_{t,GC}^{(\lambda;\beta)} = \mathbf{F}_{G_2}^\beta \exp(\lambda \mathbf{A})$ is unitary. Finally, using $(\mathbf{P} \otimes \mathbf{Q})^\mathbf{H} (\mathbf{P} \otimes \mathbf{Q}) = (\mathbf{P}^\mathbf{H} \mathbf{P}) \otimes (\mathbf{Q}^\mathbf{H} \mathbf{Q})$ with (28) gives (30). \blacksquare

Proof of Property 7: Since $(\mathbf{F}^\beta)^\mathbf{H} \mathbf{F}_{G_2}^\beta = \mathbf{W}_t^{-1}$ and $\log(\mathbf{W}_t^{-1}) = -\log(\mathbf{W}_t)$ under Assumption 1, we have

$$\tilde{\mathbf{F}}_{t,GC}^{(\lambda;\beta)} = \mathbf{F}^\beta \exp(-\lambda \log(\mathbf{W}_t)).$$

Using $\mathbf{F}^\beta = \mathbf{F}_{G_2}^\beta \exp(\log(\mathbf{W}_t))$, it follows that

$$\tilde{\mathbf{F}}_{t,GC}^{(\lambda;\beta)} = \mathbf{F}_{G_2}^\beta \exp((1-\lambda) \log(\mathbf{W}_t)) = \mathbf{F}_{t,GC}^{(1-\lambda;\beta)}.$$

Tensoring with $\mathbf{F}_{G_1}^\alpha$ yields (32). \blacksquare

APPENDIX B

PROOF OF THEOREM 1

For clarity, we reuse the notation in Section IV and write the learnable spatial order as α . Throughout this proof, the coupling parameter λ is regarded as a fixed hyperparameter and is not updated by GD.

Recall from (27) that the global GC operator admits the Kronecker form

$$\mathbf{F}_{GC}^{(\lambda;\alpha,\beta)} = \mathbf{F}_{t,GC}^{(\lambda;\beta)} \otimes \mathbf{F}_{G_1}^\alpha, \quad (40)$$

where the temporal GC basis is given in (23) by

$$\mathbf{F}_{t,GC}^{(\lambda;\beta)} = \mathbf{F}_{G_2}^\beta \exp(\lambda \log(\mathbf{W}_t(\beta))), \quad \mathbf{W}_t(\beta) = (\mathbf{F}_{G_2}^\beta)^\mathbf{H} \mathbf{F}^\beta. \quad (41)$$

By Assumption 1, $-1 \notin \sigma(\mathbf{W}_t(\beta))$, hence the principal matrix logarithm $\log(\mathbf{W}_t(\beta))$ is well-defined and Fréchet differentiable, and so is $\exp(\lambda \log(\mathbf{W}_t(\beta)))$.

Differentiability w.r.t. α . Since $\mathbf{F}_{G_1}^\alpha$ is a differentiable fractional operator with respect to its order, $\partial \mathbf{F}_{G_1}^\alpha / \partial \alpha$ exists.

TABLE VII
COMPARISON OF DENOISING PERFORMANCE (MSE/PSNR/SSIM) ON
THE REDS DATASET

Dataset	Method	Frame	MSE	PSNR	SSIM
REDS	2D-GFRFT	Frame 1	10.9443	37.74	0.9791
		Frame 2	4.2729	41.82	0.9947
		Frame 3	8.3665	38.91	0.9889
	2D-GBFRFT	Frame 1	10.7856	37.80	0.9793
		Frame 2	4.2707	41.83	0.9947
		Frame 3	8.3324	38.92	0.9890
	JFRFT	Frame 1	10.6420	37.86	0.9795
		Frame 2	4.2716	41.82	0.9947
		Frame 3	8.2394	38.97	0.9891
GC-GFRFT	Frame 1	10.4633	37.93	0.9796	
	Frame 2	4.1533	41.95	0.9948	
	Frame 3	8.3356	38.92	0.9890	
Gaussian	Frame 1	162.5462	26.02	0.7850	
	Frame 2	158.1820	26.14	0.7877	
	Frame 3	161.3213	26.05	0.7829	
Median	Frame 1	272.5740	23.78	0.6850	
	Frame 2	268.2410	23.85	0.6810	
	Frame 3	279.8108	23.66	0.6703	
NLM	Frame 1	89.5665	28.61	0.8332	
	Frame 2	89.2881	28.62	0.8302	
	Frame 3	93.9571	28.40	0.8272	

TABLE VIII
DENOISING PERFORMANCE IN TERMS OF MSE_{avg} , $PSNR_{\text{avg}}$, AND
 $SSIM_{\text{avg}}$ ON THE REDS DATASET

Dataset	Method	MSE_{avg}	$PSNR_{\text{avg}}$	$SSIM_{\text{avg}}$
REDS	2D-GFRFT	7.8612	39.49	0.9876
	2D-GBFRFT	7.7963	39.52	0.9877
	JFRFT	7.7177	39.55	0.9877
	GC-GFRFT	7.6507	39.60	0.9878
	Gaussian	160.6831	26.07	0.7852
	Median	273.5419	23.76	0.6787
	NLM	90.9372	28.54	0.8302

Using (40) and the Kronecker-product rule (with $\mathbf{F}_{t,\text{GC}}^{(\lambda;\beta)}$ independent of α), we obtain

$$\frac{\partial \mathbf{F}_{t,\text{GC}}^{(\lambda;\alpha,\beta)}}{\partial \alpha} = \mathbf{F}_{t,\text{GC}}^{(\lambda;\beta)} \otimes \frac{\partial \mathbf{F}_{G_1}^\alpha}{\partial \alpha}. \quad (42)$$

Therefore, $\mathbf{F}_{t,\text{GC}}^{(\lambda;\alpha,\beta)}$ is differentiable with respect to α .

Differentiability w.r.t. β . From (41), $\mathbf{F}_{t,\text{GC}}^{(\lambda;\beta)}$ is a product of $\mathbf{F}_{G_2}^\beta$ and $\exp(\lambda \log(\mathbf{W}_t(\beta)))$. Applying the product rule and the chain rule for Fréchet derivatives yields

$$\frac{\partial \mathbf{F}_{t,\text{GC}}^{(\lambda;\beta)}}{\partial \beta} = \frac{\partial \mathbf{F}_{G_2}^\beta}{\partial \beta} \exp(\lambda \log(\mathbf{W}_t(\beta))) \quad (43)$$

$$+ \mathbf{F}_{G_2}^\beta L_{\exp}(\lambda \log(\mathbf{W}_t(\beta)); \mathbf{E}_t(\beta)), \quad (44)$$

where $L_{\exp}(\cdot; \cdot)$ and $L_{\log}(\cdot; \cdot)$ denote the Fréchet derivatives of the matrix exponential and principal logarithm, respectively.

Moreover, differentiating $\mathbf{W}_t(\beta) = (\mathbf{F}_{G_2}^\beta)^H \mathbf{F}^\beta$ in (41) gives

$$\mathbf{W}'_t(\beta) = \left(\frac{\partial \mathbf{F}_{G_2}^\beta}{\partial \beta} \right)^H \mathbf{F}^\beta + (\mathbf{F}_{G_2}^\beta)^H \frac{\partial \mathbf{F}^\beta}{\partial \beta}, \quad (45)$$

and $\partial \mathbf{F}^\beta / \partial \beta$ exists since \mathbf{F}^β is also a differentiable fractional transform with respect to β . Hence $\partial \mathbf{F}_{t,\text{GC}}^{(\lambda;\beta)} / \partial \beta$ exists.

Finally, by (40),

$$\frac{\partial \mathbf{F}_{\text{GC}}^{(\lambda;\alpha,\beta)}}{\partial \beta} = \frac{\partial \mathbf{F}_{t,\text{GC}}^{(\lambda;\beta)}}{\partial \beta} \otimes \mathbf{F}_{G_1}^\alpha, \quad (46)$$

which establishes differentiability with respect to β .

Differentiability of the objective. By Property 6 in Section IV, $\mathbf{F}_{\text{GC}}^{(\lambda;\alpha,\beta)}$ is unitary for $\lambda \in [0, 1]$, so its inverse exists and satisfies $(\mathbf{F}_{\text{GC}}^{(\lambda;\alpha,\beta)})^{-1} = (\mathbf{F}_{\text{GC}}^{(\lambda;\alpha,\beta)})^H$. Therefore, the mapping

$$\mathbf{y} \mapsto (\mathbf{F}_{\text{GC}}^{(\lambda;\alpha,\beta)})^{-1} \mathbf{H}_{\text{GC}} \mathbf{F}_{\text{GC}}^{(\lambda;\alpha,\beta)} \mathbf{y}$$

is a composition of differentiable matrix functions and linear operators in $(\alpha, \beta, \mathbf{h})$. Consequently, the loss in (35) is differentiable with respect to $(\alpha, \beta, \mathbf{h})$ for fixed admissible λ . ■

REFERENCES

- [1] C. Cheng, Y. Chen, Y. J. Lee, and Q. Sun, "SVD-based graph Fourier transforms on directed product graphs," *IEEE Trans. Signal Inf. Process. Netw.*, vol. 9, pp. 531–541, 2023.
- [2] P. Ferrer-Cid, J. M. Barcelo-Ordinas, and J. Garcia-Vidal, "Graph signal reconstruction techniques for iot air pollution monitoring platforms," *IEEE Internet Things J.*, vol. 9, no. 24, pp. 25 350–25 362, 2022.
- [3] H. Zhao, C. Li, and W. Xiang, "Data-reuse adaptive algorithms for graph signal estimation over sensor network," *IEEE Sens. J.*, vol. 24, no. 4, pp. 5086–5096, 2024.
- [4] C. Koke and G. Kutyniok, "Graph scattering beyond wavelet shackles," in *Proc. Adv. Neural Inf. Process. Syst. (NeurIPS)*, vol. 35, 2022, pp. 30 219–30 232.
- [5] J. Jiang, H. Feng, D. B. Tay, and S. Xu, "Theory and design of joint time-vertex nonsubsampling filter banks," *IEEE Trans. Signal Process.*, vol. 69, pp. 1968–1982, 2021.
- [6] F. Schwock, J. Bloch, L. Atlas, S. Abadi, and A. Yazdan-Shahmorad, "Estimating and analyzing neural information flow using signal processing on graphs," in *Proc. IEEE Int. Conf. Acoust., Speech, Signal Process. (ICASSP)*, 2023, pp. 1–5.
- [7] H. Mohammadi and W. Karwowski, "Graph neural networks in brain connectivity studies: Methods, challenges, and future directions," *Brain Sci.*, vol. 15, no. 1, p. 17, 2024.
- [8] W. Hu, J. Pang, X. Liu, D. Tian, C.-W. Lin, and A. Vetro, "Graph signal processing for geometric data and beyond: Theory and applications," *IEEE Trans. Multimedia*, vol. 24, pp. 3961–3977, 2021.
- [9] S. Sardellitti and S. Barbarossa, "Topological signal processing over generalized cell complexes," *IEEE Trans. Signal Process.*, vol. 72, pp. 687–700, 2024.
- [10] Z. Fu, Y. Lin, D. Yang, and S. Yang, "Fractional Fourier transforms meet Riesz potentials and image processing," *SIAM J. Imaging Sci.*, vol. 17, no. 1, pp. 476–500, 2024.
- [11] S. Yang, Z. Fu, D. Yang, Y. Lin, and Z. Li, "Refining image edge detection via linear canonical Riesz transforms," *SIAM J. Imaging Sci.*, 2026, Early Access, Doi: 10.1137/25M1752225.
- [12] D. I. Shuman, S. K. Narang, P. Frossard, A. Ortega, and P. Vandergheynst, "The emerging field of signal processing on graphs: Extending high-dimensional data analysis to networks and other irregular domains," *IEEE Signal Process. Mag.*, vol. 30, no. 3, pp. 83–98, 2013.
- [13] A. Sandryhaila and J. M. F. Moura, "Discrete signal processing on graphs," *IEEE Trans. Signal Process.*, vol. 61, no. 7, pp. 1644–1656, 2013.
- [14] A. Sandryhaila and J. M. F. Moura, "Discrete signal processing on graphs: Frequency analysis," *IEEE Trans. Signal Process.*, vol. 62, no. 12, pp. 3042–3054, 2014.

- [15] L. Stanković, D. Mandić, M. Daković, B. Scalzo, M. Brajović, E. Sejdić, and A. G. Constantinides, "Vertex-frequency graph signal processing: A comprehensive review," *Digit. Signal Process.*, vol. 107, p. 102802, 2020.
- [16] A. Gavili and X.-P. Zhang, "On the shift operator, graph frequency, and optimal filtering in graph signal processing," *IEEE Trans. Signal Process.*, vol. 65, no. 23, pp. 6303–6318, 2017.
- [17] R. R. Coifman and M. Maggioni, "Diffusion wavelets," *Appl. Comput. Harmon. Anal.*, vol. 21, no. 1, pp. 53–94, 2006.
- [18] D. K. Hammond, P. Vandergheynst, and R. Gribonval, "Wavelets on graphs via spectral graph theory," *Appl. Comput. Harmon. Anal.*, vol. 30, no. 2, pp. 129–150, 2011.
- [19] S. K. Narang and A. Ortega, "Perfect reconstruction two-channel wavelet filter banks for graph structured data," *IEEE Trans. Signal Process.*, vol. 60, no. 6, pp. 2786–2799, 2012.
- [20] S. Deutsch, A. Ortega, and G. Medioni, "Manifold denoising based on spectral graph wavelets," in *Proc. IEEE Int. Conf. Acoust., Speech, Signal Process. (ICASSP)*, 2016, pp. 4673–4677.
- [21] S. Chen, R. Varma, A. Sandryhaila, and J. Kovačević, "Discrete signal processing on graphs: Sampling theory," *IEEE Trans. Signal Process.*, vol. 63, no. 24, pp. 6510–6523, 2015.
- [22] Y. Tanaka and Y. C. Eldar, "Generalized sampling on graphs with subspace and smoothness priors," *IEEE Trans. Signal Process.*, vol. 68, pp. 2272–2286, 2020.
- [23] J. Shi and J. M. F. Moura, "Graph signal processing: Dualizing gsp sampling in the vertex and spectral domains," *IEEE Trans. Signal Process.*, vol. 70, pp. 2883–2898, 2022.
- [24] E. Isufi, A. Loukas, A. Simonetto, and G. Leus, "Autoregressive moving average graph filtering," *IEEE Trans. Signal Process.*, vol. 65, no. 2, pp. 274–288, 2017.
- [25] D. B. Tay and J. Jiang, "Time-varying graph signal denoising via median filters," *IEEE Trans. Circuits Syst. II, Exp. Briefs*, vol. 68, no. 3, pp. 1053–1057, 2020.
- [26] E. Bayram, P. Frossard, E. Vural, and A. Alatan, "Analysis of airborne LiDAR point clouds with spectral graph filtering," *IEEE Geosci. Remote Sens. Lett.*, vol. 15, no. 8, pp. 1284–1288, 2018.
- [27] A. Ortega, *Introduction to Graph Signal Processing*. Cambridge Univ. Press, 2022.
- [28] Y. Wang and B. Li, "The fractional Fourier transform on graphs: Sampling and recovery," in *Proc. IEEE Int. Conf. Signal Process. (ICSP)*, 2018, pp. 1103–1108.
- [29] Y. Wang, B. Li, and Q. Cheng, "The fractional Fourier transform on graphs," in *Proc. Asia-Pacific Signal Inf. Process. Assoc. Annu. Summit Conf. (APSIPA ASC)*, 2017, pp. 105–110.
- [30] L. B. Almeida, "The fractional Fourier transform and time-frequency representations," *IEEE Trans. Signal Process.*, vol. 42, no. 11, pp. 3084–3091, 2002.
- [31] T. Alikashişoğlu, B. Kartal, and A. Koç, "Graph fractional Fourier transform: A unified theory," *IEEE Trans. Signal Process.*, vol. 72, pp. 3834–3850, 2024.
- [32] D. Wei and Z. Yan, "Generalized sampling of graph signals with the prior information based on graph fractional Fourier transform," *Signal Process.*, vol. 214, p. 109263, 2024.
- [33] E. Koç, T. Alikashişoğlu, A. C. Aras, and A. Koç, "Trainable fractional Fourier transform," *IEEE Signal Process. Lett.*, vol. 31, pp. 751–755, 2024.
- [34] F. Şahinuç and A. Koç, "Fractional Fourier transform meets transformer encoder," *IEEE Signal Process. Lett.*, vol. 29, pp. 2258–2262, 2022.
- [35] T. Kurokawa, T. Oki, and H. Nagao, "Multi-dimensional graph Fourier transform," *arXiv preprint arXiv:1712.07811*, 2017.
- [36] A. Natali, E. Isufi, and G. Leus, "Forecasting multi-dimensional processes over graphs," in *Proc. IEEE Int. Conf. Acoust., Speech, Signal Process. (ICASSP)*, 2020, pp. 5575–5579.
- [37] R. A. Varma and J. Kovačević, "Sampling theory for graph signals on product graphs," in *Proc. IEEE Global Conf. Signal Inf. Process. (GlobalSIP)*, 2018, pp. 768–772.
- [38] F. Yan and B. Li, "Multi-dimensional graph fractional Fourier transform and its application to data compression," *Digit. Signal Process.*, vol. 129, p. 103683, 2022.
- [39] A. Loukas and D. Foucard, "Frequency analysis of time-varying graph signals," in *Proc. IEEE Global Conf. Signal Inf. Process. (GlobalSIP)*, 2016, pp. 346–350.
- [40] F. Grassi, A. Loukas, N. Perraudin, and B. Ricaud, "Time-vertex signal processing: Framework, analytical extensions, and applications," *IEEE Trans. Signal Process.*, vol. 66, no. 3, pp. 817–831, 2018.
- [41] T. Alikashişoğlu, B. Kartal, E. Özgünay, and A. Koç, "Joint time-vertex fractional Fourier transform," *Signal Process.*, vol. 233, p. 109944, 2025.
- [42] T. Alikashişoğlu, B. Kartal, and A. Koç, "Wiener filtering in joint time-vertex fractional Fourier domains," *IEEE Signal Process. Lett.*, vol. 31, pp. 1319–1323, 2024.
- [43] Z. Yan and Z. Zhang, "Trainable joint time-vertex fractional Fourier transform," *Digit. Signal Process.*, p. 105909, 2026.
- [44] S. Nijhawan, A. Gupta, K. Appaiah, R. Vaze, and N. Karamchandani, "Flag manifold-based precoder interpolation techniques for MIMO-OFDM systems," *IEEE Trans. Commun.*, vol. 69, no. 7, pp. 4347–4359, 2021.
- [45] P. Mehta, A. Kumar, S. R. B. Pillai, and K. Appaiah, "Matrix unimodular precoder interpolation for MIMO-OFDM wireless communication systems," *IEEE Commun. Lett.*, vol. 27, no. 11, pp. 3038–3042, 2023.
- [46] R. Sun, C. Wang, A.-A. Lu, X. Gao, and X.-G. Xia, "Precoder design for massive MIMO downlink with matrix manifold optimization," *IEEE Trans. Signal Process.*, vol. 72, pp. 1065–1080, 2024.
- [47] C. Ozturk, H. M. Ozaktas, S. Gezici, and A. Koç, "Optimal fractional Fourier filtering for graph signals," *IEEE Trans. Signal Process.*, vol. 69, pp. 2902–2912, 2021.
- [48] T. Lin and S. Bourennane, "Survey of hyperspectral image denoising methods based on tensor decompositions," *EURASIP J. Adv. Signal Process.*, vol. 2013, no. 1, p. 186, 2013.
- [49] S. Gannot and I. Cohen, "Adaptive beamforming and postfiltering," in *Springer Handbook of Speech Process.* Springer, 2008, pp. 945–978.
- [50] J. Hara, Y. Tanaka, and Y. C. Eldar, "Graph signal sampling under stochastic priors," *IEEE Trans. Signal Process.*, vol. 71, pp. 1421–1434, 2023.
- [51] A. C. Yağan and M. T. Özgen, "Spectral graph based vertex-frequency Wiener filtering for image and graph signal denoising," *IEEE Trans. Signal Inf. Process. Netw.*, vol. 6, pp. 584–598, 2020.
- [52] E. Isufi, A. Loukas, M. Perlmutter, A. Ribeiro, and G. Leus, "Graph filters for signal processing and machine learning," *IEEE Trans. Signal Process.*, vol. 72, pp. 4745–4781, 2024.
- [53] G. B. Ribeiro and J. B. Lima, "Graph signal processing in a nutshell," *J. Commun. Inf. Syst.*, vol. 33, no. 1, 2018.
- [54] K. Qiu, X. Mao, X. Shen, X. Wang, T. Li, and Y. Gu, "Time-varying graph signal reconstruction," *IEEE J. Sel. Topics Signal Process.*, vol. 11, no. 6, pp. 870–883, 2017.
- [55] X. Mao and Y. Gu, "Time-varying graph signals reconstruction," in *Vertex-Frequency Analysis of Graph Signals*. Springer, 2018, pp. 293–316.
- [56] H. M. Ozaktas and D. Mendlovic, "Fourier transforms of fractional order and their optical interpretation," *Opt. Commun.*, vol. 101, no. 3-4, pp. 163–169, 1993.
- [57] D. Mendlovic and H. M. Ozaktas, "Fractional Fourier transforms and their optical implementation: I," *J. Opt. Soc. Amer. A*, vol. 10, no. 9, pp. 1875–1881, 1993.
- [58] H. M. Ozaktas and M. A. Kutay, "The fractional Fourier transform," in *Proc. Eur. Control Conf. (ECC)*, 2001, pp. 1477–1483.
- [59] C. Candan, M. A. Kutay, and H. M. Ozaktas, "The discrete fractional Fourier transform," *IEEE Trans. Signal Process.*, vol. 48, no. 5, pp. 1329–1337, 2000.
- [60] T. S. Huang, G. J. Yang, and G. Y. Tang, "A fast two-dimensional median filtering algorithm," *IEEE Trans. Acoust., Speech, Signal Process.*, vol. 27, no. 1, pp. 13–18, 1979.
- [61] T. N. Kipf and M. Welling, "Semi-supervised classification with graph convolutional networks," in *Proc. Int. Conf. Learn. Represent. (ICLR)*, 2017.
- [62] P. Veličković, G. Cucurull, A. Casanova, A. Romero, P. Liò, and Y. Bengio, "Graph attention networks," in *Proc. Int. Conf. Learn. Represent. (ICLR)*, 2018.
- [63] M. Defferrard, X. Bresson, and P. Vandergheynst, "Convolutional neural networks on graphs with fast localized spectral filtering," in *Proc. Adv. Neural Inf. Process. Syst. (NeurIPS)*, 2016, pp. 3844–3852.
- [64] S. Nah, T. H. Kim, and K. M. Lee, "Deep multi-scale convolutional neural network for dynamic scene deblurring," in *Proc. IEEE Conf. Comput. Vis. Pattern Recognit. (CVPR)*, 2017, pp. 3803–3814.
- [65] S. W. Zamir, A. Arora, S. Khan, M. Hayat, F. S. Khan, M.-H. Yang, and L. Shao, "Restormer: Efficient transformer for high-resolution image restoration," in *Proc. IEEE/CVF Conf. Comput. Vis. Pattern Recognit. (CVPR)*, 2022, pp. 5728–5739.
- [66] L. Chen, X. Chu, X. Zhang, and J. Sun, "Simple baselines for image restoration," in *Proc. Eur. Conf. Comput. Vis. (ECCV)*, 2022, pp. 48–63.